Modulating the open pore structure of hard carbons derived from wood for sodium-ion battery anodes

Li Menglong[1], Gong Jun[1,*], Li Jinming[2], Xie Haipeng[2], Li Yejun[3,*]

(1. *School of Mechanical Engineering*, *Hunan University of Science and Technology*, *Xiangtan* 411201, *China*;
2. *Hunan Key Laboratory of Nanophotonics and Devices*, *School of Physics*, *Central South University*, *Changsha* 410083, *China*;
3. *School of Materials Science and Engineering*, *Central South University*, *Changsha* 410083, *China*)

Abstract: Hard carbon (HC) derived from renewable biomass is a promising anode material for sodium-ion batteries (SIBs). However, controlling the structure of hard carbon so that it has a high energy density, favorable rate performance, and cycling stability is still a challenge. We propose a strategy to control the open pore structure of hard carbon derived from wood for sodium-ion storage by the addition of sodium carbonate under carbonization at 1100 °C. The resulting HC has an increased interlayer spacing, and a more uniform open pore distribution (2–3 nm) with a high slope capacity, thereby enabling efficient sodium-ion transport and storage. The HC anode has a reversible capacity of 326 mAh g^{-1} at a current density of 30 mA g^{-1}, and maintains a reversible capacity of 270 mAh g^{-1} at 1 A g^{-1} and a capacity of 68 mAh g^{-1} even at 10 A g^{-1} during rate performance tests. After 300 cycles, it retains 76.7% (207 mAh g^{-1}) of its capacity at 1.0 A g^{-1}. In situ Raman spectroscopy and the galvanostatic intermittent titration testing results reveal an adsorption-intercalation-filling sodium storage mechanism. This work provides a strategy to optimize the open pore structure of biomass derived hard carbon for high performance sodium ion storage.

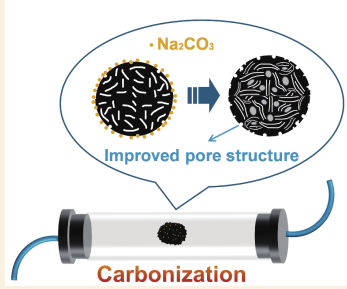

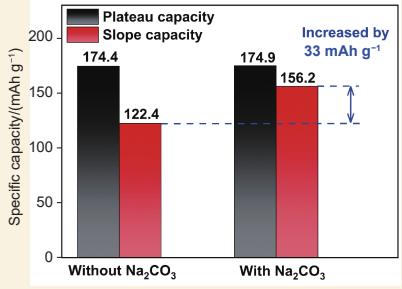

Key words: Sodium-ion batteries; Hard carbon; Biomass; Pore structure

1 Introduction

Due to a significant complement of sodium-ion batteries (SIBs) to lithium-ion batteries (LIBs), various materials are currently being employed as anode materials for SIBs, including carbon materials[1], alloys[2], transition metal oxides[3], sulphides[4] and others. Carbon-based materials, with the economic, stable and mature manufacture advantages, have attracted considerable attention[5]. Although the operating mechanism is fundamentally consistent with that of LIBs, the larger radius of Na^+ limits the application of graphite in SIBs[6], where hard carbon is widely used. Biomass serves as a cost-effective precursor for preparation of hard carbons because of its high carbon content, affordability and scalability, making it a better option compared to costly polymer resins and non-renewable fossil fuels[6–8].

Generally, the storage pore types of hard carbons for sodium ions encompass open and closed pores (2–5 nm), wherein open pores comprise micropores (<2 nm), mesopores (2–50 nm), and macropores (>50 nm)[9–10]. To optimize the pore structure of hard carbons, several strategies have been developed, including the regulation of biomass precursor components[11], the optimization of pyrolysis conditions[12], the templating methods[13], and surface coating techniques[14-15]. It should be noted that the recent research has mainly focused on the modulation of closed pores, which is closely related to the plateau capacity of hard carbons, where sodium ions fill the closed pores or even form quasi-metallic sodium clusters to provide

Received: November 30, 2025
Revised: March 15, 2026
Accepted: March 17, 2026

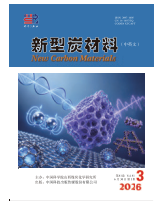

the primary reversible capacity[16–18]. However, an excessive bias towards closed-pore formation will yield extremely high plateau capacity and high energy density, at the same time will suffer from insufficient ion transport pathways, poor rate performance, limited electrolyte wettability, and weak buffering capacity against volume changes during cycling[19]. The open pore structures, on the other hand, are believed to not only offer adsorption sites for sodium ions and contribute to the slope capacity, but also serve as an electrolyte reservoir, which facilitate rapid ion transport and improves rate performance[20-22]. Previous studies have demonstrated that carbon dioxide in carbonization can facilitate the formation of numerous closed pores in hard carbons[23]. During the CO_2 etching process, open pores are initially created within the carbon matrix, which are subsequently reorganized into closed pores through in-situ reconstruction during high-temperature carbonization. This CO_2-assisted pore modulation strategy effectively enhances both the diameter and the volumetric capacity of closed pores in the resulting hard carbons. Therefore, the pore structures, including open and closed pores, can be effectively tuned through rational control of the carbonization temperature and the amount of carbon dioxide.

Herein, we proposed a strategy to tailor the porous architecture of wood-derived hard carbon, aiming to achieve high-performance anode materials for SIBs. By mixing the wooden precursor with Na_2CO_3, it releases CO_2 gas under high-temperature treatment, which increases both porosity and interlayer spacing of the obtained hard carbons[24]. By modulating the ratio of Na_2CO_3 to wood and the carbonization temperature, the open pore structures of the obtained hard carbons can be tuned, where the slope capacity of the obtained hard carbons is significantly enhanced with an improved performance for sodium ion storage. The sodium storage mechanism of the obtained hard carbons, following the "adsorption-intercalation-pore filling" sequence, was confirmed by in-situ Raman spectroscopy and galvanostatic intermittent titration technique (GITT). The present work offers a simple and feasible strategy to modify the open pore structures for the preparation of wood-derived hard carbon anodes for high performance SIBs.

2 Experimental

2.1 Material preparation

The linden wood precursor purchased from Hunan BobSun New Materials Co. Ltd. was subsequently pulverized and sieved through a 300-mesh. Then, 3 g of the wood precursors was mixed with 0, 0.3, 0.6 and 0.9 g of Na_2CO_3 in glass bottles (with a ratio of 10%, 20% and 30%, respectively), respectively, and stirred with an appropriate amount of deionized water for 2 h. The mixture was then dried in an air-blown drying oven, which was transferred to a quartz boat and carbonized under an argon atmosphere at a heating rate of 5 °C/min to a target temperature for 2 h. Finally, the obtained sample was immersed in 2 mol L^{-1} hydrochloric acid under stirring for 12 h, thoroughly rinsed with deionized water until a neutral pH (~ 7) was achieved, and subsequently dried in a vacuum oven. The resulting products were labeled as W-X-Y, where X indicates the mass percentage of the added Na_2CO_3 (0, 10%, 20% and 30%), and Y denotes the carbonization temperature (900, 1100 and 1300 °C). For instance, W-20%-1100 corresponds to the sample carbonized at 1100 °C with 20% Na_2CO_3.

2.2 Material characterization

The microcrystalline structure of the samples was analyzed using a confocal micro-Raman spectrometer (inVia™ Qontor®, Renishaw plc, UK) with a laser wavelength of 532 nm. The surface morphology of the materials was characterized using scanning electron microscope (SEM, JEM-F200, JEOL Ltd., Japan). The specific surface area and open pore size distribution were measured with a fully automated surface area and porosity analyzer (Micromeritics ASAP 2460). The detailed crystalline structure was further examined by X-ray diffraction (XRD, Empyrean SmartLab SE, Malvern Panalytical, the Netherlands).

2.3 In-situ Raman measurements

The slurries of the prepared samples were coated on the copper foil and dried overnight, which was then

assembled with Na foil in a CR2025 battery case with small holes. The in-situ Raman measurements of electrodes were performed with Renishaw Raman spectroscopy with a 532 nm laser excitation. The discharge/charge processes were controlled by CHI760E at 300 mA g^{-1}.

2.4 Electrochemical measurements

CR2025-type coin cells were assembled for electrochemical performance evaluation. The working electrode was composed of 80% active material, 10% conductive carbon black, and 10% polyvinylidene fluoride (PVDF) binder, which was dissolved in N-Methyl pyrrolidone (NMP) solvent. The mixture was thoroughly ground in a mortar to form a homogeneous slurry, which was then coated onto a copper foil using a doctor blade. The coated electrode was dried at 80 °C for 12 h in a vacuum oven and subsequently punched into circular disks with a diameter of 12 mm. The mass loading of the active material was controlled at approximately 1-2 mg cm^{-2}, and the electrolyte solution is 1 mol L^{-1} $NaPF_6$ in diglyme: DME=1∶1 (volume fraction). Glass fibre paper was used as a diaphragm (Whatman GF/D). The CR2025-type coin cells were then assembled in an argon-filled glove box with rigorously controlled atmospheric conditions (H_2O, O_2 < 1.0×10^{-7}, *v*/*v*). Electrochemical measurements were carried out using a Neware battery test system at a constant temperature of 25 °C, within a voltage window of 0.01–3.0 V. Cyclic voltammetry (CV) and electrochemical impedance spectroscopy (EIS) were performed on a CHI760E electrochemical workstation. The EIS measurements were carried out in a frequency range from 100 kHz to 0.01 Hz with an amplitude of 5 mV. Galvanostatic intermittent titration technique (GITT) was employed to determine the ionic diffusion coefficients of the materials, with a pulse current of 0.1 C, a pulse duration of 10 min, and a relaxation time of 2 h. All measurements were conducted within a voltage range of 0.01–3.0 V.

3 Results and discussion

A schematic diagram of the experimental process is depicted in Fig. 1, where a systematic investigation of the influence of Na_2CO_3 addition (10%, 20%, 30%) (Table S1) on the performance of hard carbon anodes reveals that their overall sodium storage performance is best at 20%. SEM image reveals that the sizes of the hard carbon particles are about 12 μm and there is no significant difference of the surface morphology for different samples (Fig. S1).

Raman spectroscopy was employed to characterize the degree of graphitization of the hard carbons. As shown in Fig. 2a, the addition of Na_2CO_3 induces an increase of disorder in the sample as revealed by the ratio of *D* peak to *G* peak (I_D/I_G). As the carbonization temperature increases, the I_D/I_G ratio decreases, indicating the gradual increase of graphitization degree of the samples with the carbonization temperature. XRD was further carried out to characterize the structural features of the hard carbons (Fig. 2b). Two broad diffraction signals are found at approximately

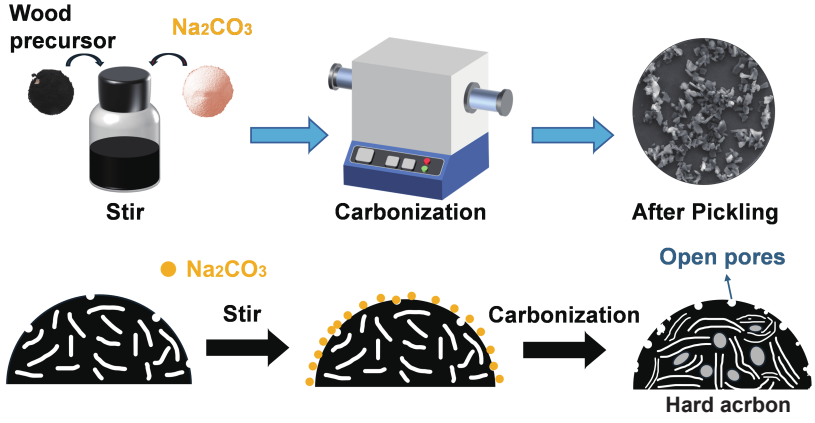

Fig. 1 Schematic diagram of the experimental process

23º and 43º, corresponding to the (002) and (100) diffraction peaks of amorphous carbon, respectively[25]. A diffraction peak at approximately 26.5º appears with increasing the carbonization temperature. Compared to W-1100, the diffraction peaks of W-20%-1100 become broader, and its (002) peak shifts towards lower angles, indicating an increase in the average interlayer spacing. The interlayer spacing (d_{002}), the average size of graphene layers (L_a), and the grain size along the c-axis (L_c) were estimated with the Bragg equation (Eq. S1) and the Scherrer formula (Eq. S2), as shown in Table 1. At the same carbonization temperature, the interlayer spacing of W-1100 is 0.390 nm, while that of W-20%-1100 increases to 0.399 nm, accompanied by reduced L_c and L_a values. This indicates that Na_2CO_3 incorporation increases the interlayer spacing and impedes graphitization during high-temperature processing, which will provide wider pathways for sodium ion migration. As the carbonization temperature increases, the interlayer spacing decreases from 0.397 nm of W-20%-900 to 0.382 nm of W-20%-1300, while the L_c and L_a values progressively rise, suggesting an increase of graphitization degree.

As shown in Fig. S2, the locally ordered carbon layers are classified as a graphite-like phase (green oval marker), and the carbon layers are stacked to form more closed pores (yellow squares marker), where some of the carbon layers that suddenly break and are spaced apart are classified as open pores (red triangle marker). It is clear that W-20%-1100 with the addition of Na_2CO_3 yields a more disordered carbon layer structure and more open pores compared to W-1100 sample. This is because the gases produced by the high-temperature decomposition of Na_2CO_3 leads to the formation of a rich pore structure on the surface of the hard carbon, which provides wood-based hard carbon with abundant Na^+ storage sites. Further-

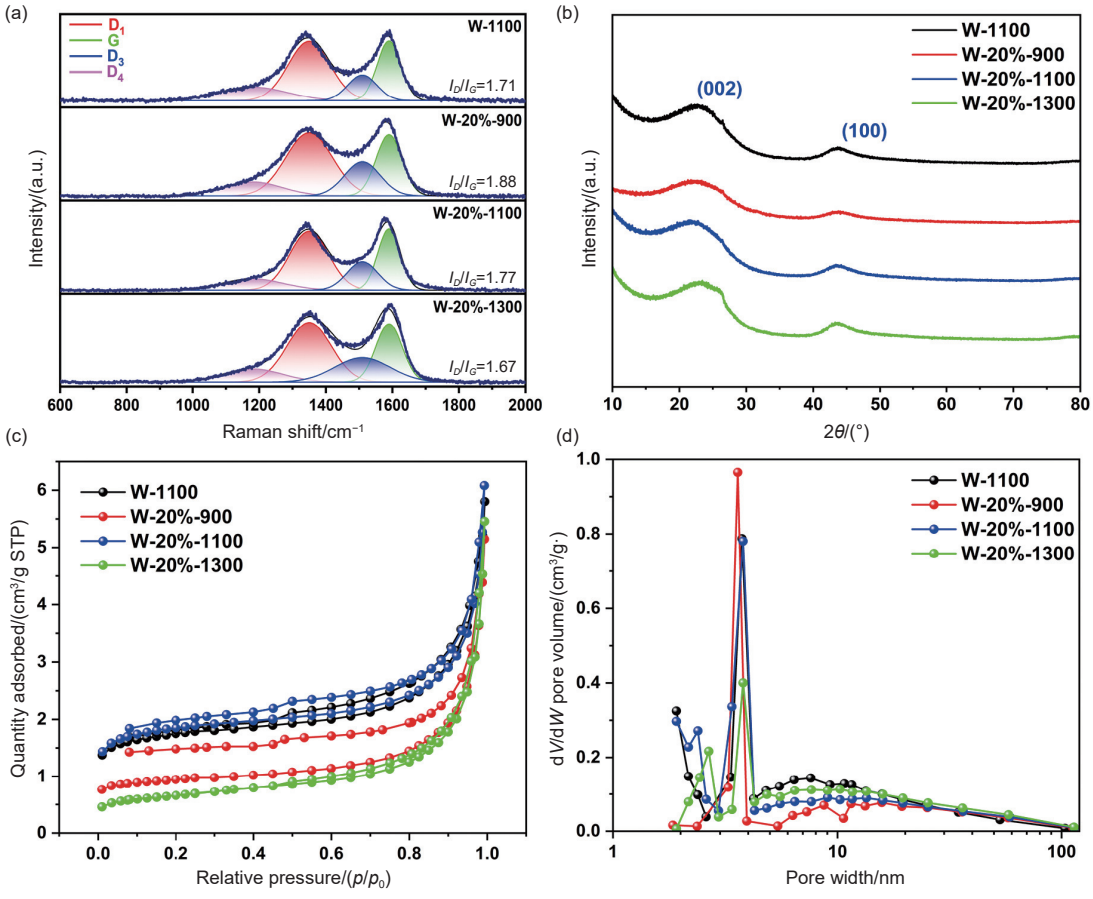

Fig. 2 (a) Raman spectra; (b) XRD patterns; (c) N_2 adsorption and desorption isotherms and (d) the pore size distribution curves of the prepared samples

Table 1 Structural parameters of different samples

Samples	d_{002}/nm	L_c/nm	L_a/nm	S_{BET} ($m^2\ g^{-1}$)	Total pore volume/($mm^3\ g^{-1}$)
W-1100	0.390±0.005	0.635±0.001	2.374±0.004	6.58±0.012	8.97±0.06
W-20%-900	0.397±0.007	0.493±0.001	1.782±0.003	3.54±0.013	7.96±0.02
W-20%-1100	0.399±0.007	0.558±0.001	2.003±0.005	6.98±0.013	9.40±0.06
W-20%-1300	0.382±0.010	0.589±0.001	2.439±0.005	2.35±0.008	8.44±0.09

more, increasing of the carbonization temperature also leads to the formation of graphite-like phases. This is consistent with the results from Raman and XRD.

The specific surface area and pore size distribution of the prepared hard carbon were determined by N_2 adsorption, where all samples exhibit the Type IV adsorption-desorption isotherms (Fig. 2c). It is noteworthy that the hysteresis loop of W-20%-900 is not fully closed, with no distinct saturation adsorption plateau with highly irregular pore structure, suggesting insufficient carbonization[26]. Compared to W-1100, aside from the main peak at 3.5 nm, W-20%-1100 exhibits a clear increase in pore volume around 2.3 nm, suggesting the formation of open pores due to the released gas molecules from the high-temperature decomposition of Na_2CO_3. This is also reflected by the slightly increased specific surface area and total pore volume of W-20%-1100 (Table 1). With the increase of the carbonization temperature, W-20%-1300 exhibits an overall rightward shift in peak position and a general decrease in peak intensity, indicating enlarged pore sizes and reduced pore numbers at higher carbonization temperature[27]. In this sense, W-20%-1100 will provide abundant active sites for Na^+ storage with enhanced diffusion kinetics.

The electrochemical performance of the prepared samples was evaluated in sodium half-cells using metallic sodium as the counter/reference electrode, within a voltage range of 0.01–3.0 V. In the dQ/dV curves of the hard carbon electrodes, a reduction peak at approximately 1.25 V is observed only during the 1st cycle (Fig. 3a), which can be attributed to the formation of a solid electrolyte interphase (SEI) film. The irreversible peak area of W-20%-1100 is smaller than those of the other samples, indicating suppressed side reactions between surface defects and the electrolyte (Fig. S3). The weak and broad reduction peak between 1.0 and 0.5 V demonstrates the adsorption behavior of Na^+ at the surface sites on the electrode[28]. Additionally, a pair of reversible redox peaks observed at approximately 0.1 V corresponds to the intercalation/filling and extraction of Na^+.

To understand the effect of the pore structure of the samples on the performance of the sodium ion storage, the galvanostatic charge–discharge (GCD) curves were measured. As observed in the initial charge-discharge cycles at a current density of 30 mA g^{-1} (Fig. 3b and S4), the sodium storage capacities of all samples generally consist of 2 typical regions: a plateau region between 0.01 and 0.1 V, corresponding to sodium storage in interlayer intercalation and closed pores, and a sloping region between 0.1 and 3.0 V, related to Na^+ adsorption at surface defects and open pores[29]. The initial discharge capacity and charge capacity of W-1100 are 429 and 291 mAh g^{-1} (Table S2), respectively. These values of W-20%-900 and W-20%-1300 after the addition of Na_2CO_3 become lowered. However, W-20%-1100 shows the highest initial discharge capacity and charge capacity (460 and 326 mAh g^{-1}) along with a slight increase in ICE to 71% among all samples. A detailed analysis was carried on the plateau capacity and slope capacity of the 2nd cycle for all samples (Fig. 3c). It is interesting to note that the plateau capacities of both W-1100 and W-20%-1100 are very close and the increased capacity of W-20%-1100 is mainly contributed by the slope region, with an increase from 122 to 156 mAh g^{-1}. This improvement can be attributed to the induced open pores, surface defects and increased interlayer spacing with the addition of Na_2CO_3 for W-20%-1100, which provide more sites for sodium ion storage. As the carbonization

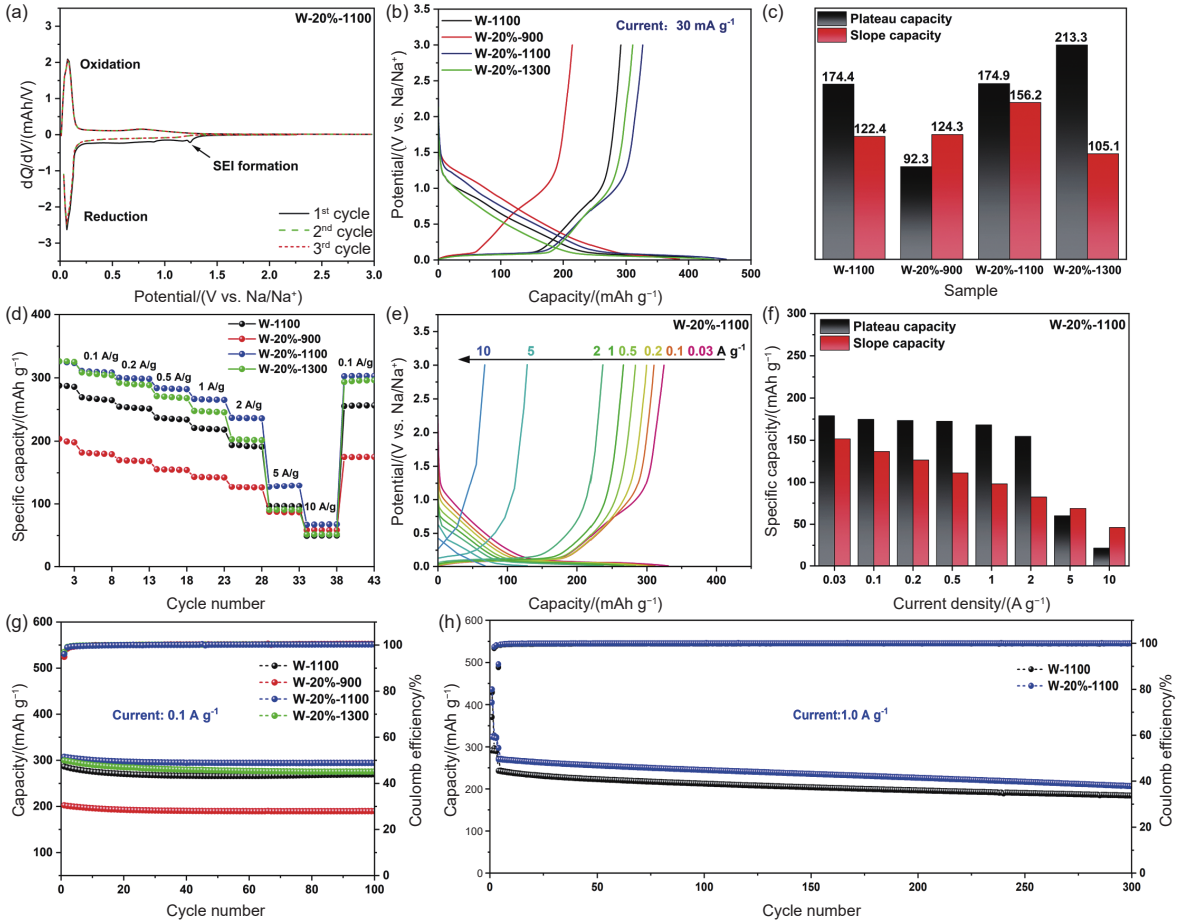

Fig. 3 (a) dQ/dV curve for W-20%-1100. (b) GCD curves of different samples in the 1st cycle at a current density of 30 mA g^{-1}. (c) Capacity contribution of the 2nd cycle for different samples. (d) Rate performance of different samples. (e) GCD curves and (f) capacity contribution of W-20%-1100 at different current densities. (g) Cycling stability of different samples at 0.1 A g^{-1}. (h) Cycling stability of W-1100 and W-20%-1100 at 1 A g^{-1}

temperature goes up, the graphitization degree increases, giving rise to short-range ordered graphite-like domains and closed-pore structures. Although the balance between ion diffusion pathways and active site density enhance the plateau capacity of W-20%-1300[11,27], the reduced open pore volume significantly reduces its slope capacity, which eventually results in a lowered total capacity.

Aside from these, in comparison with the other samples, W-20%-1100 exhibits exceptional rate performance (Fig. 3d), with reversible charge capacities of 326, 311, 300, 284, 270, 237, 127 and 68 mAh g^{-1} at current densities of 0.03, 0.1, 0.2, 0.5, 1, 2, 5 and 10 A g^{-1}, respectively. When the current density is restored to 0.1 A g^{-1}, W-20%-1100 still delivers a reversible charge capacity of 303 mAh g^{-1} (Fig. 3e), about 92.8% of its initial value. This outstanding performance can be attributed to the rapid adsorption and efficient diffusion of Na^+ within the rich open porous structure and on surface defects. In comparison, W-1100 only delivers reversible charge capacities of 287, 269, 254, 237, 221, 194, 97 and 49 mAh g^{-1} at current densities of 0.03, 0.1, 0.2, 0.5, 1, 2, 5 and 10 A g^{-1} (Fig. 3d and S5a), respectively. It is interesting to note that the capacity decay at high current densities primarily stems from the loss of plateau capacity (Fig. 3f and S5b), which may be attributed to significant polarization during sodium deposition/stripping within closed pores at high rates, thereby causing irreversible capacity loss[28].

The cycling performance of the samples was tested at current densities of 0.1 A g^{-1} (Fig. 3g and S6), 0.5 A g^{-1} (Fig. S7-8) and 1 A g^{-1} (Fig. 3h and S9-10). To be specific, W-20%-1100 exhibits capacity re-

tention rates of 94.5% (294 mAh g^{-1}) after 100 cycles at 0.1 A g^{-1}, and of 81.3% (231 mAh g^{-1}) after 300 cycles at 0.5 A g^{-1}, outperforming the other samples. Even more impressively, W-20%-1100 retains a reversible specific capacity of 207 mAh g^{-1} at 1 A g^{-1} after 300 cycles, with a capacity retention rate of 76.7%. Compared to W-1100, it offers a capacity increase of 23 mAh g^{-1} with a more stable charge-discharge curve. In general, W-20%-1100 exhibits higher reversible charge capacity and initial Coulombic efficiency, along with superior comprehensive electrochemical performance, compared with the wood-derived hard carbons reported in the literatures (Table 2).

To investigate the underlying mechanism of Na^+ storage in the hard carbons, CV and EIS were employed to examine the internal changes occurring during Na^+ storage. Each sample was scanned three times at a rate of 0.1 mV s^{-1} within the voltage range of 0.01–3 V. As shown in Fig. 4a-b, both W-1100 and W-20%-1100 exhibit an irreversible peak at around 1.25 V during the reduction process, corresponding to the electrolyte decomposition and SEI film formation. Two peaks are observed at approximately 0.01 and 0.15 V, corresponding to the Na^+ intercalation within the graphitic layers and pseudo-metallic sodium filling in the micropores, respectively[36]. The CV curves for the initial 3 cycles show nearly overlap (Fig. 4a-b, and S11), demonstrating excellent reversibility in the electrochemical processes[37].

$$i = av^b \quad (1)$$

$$i(v) = k_1 v + k_2 v^{\frac{1}{2}} \quad (2)$$

CV curves at different scan rates are shown in Fig. 4c-d and S12-13, where the electrochemical storage mechanism of Na^+ during charge-discharge cycles can be described by Eq. (1) and (2). W-1100 and W-20%-1100 exhibit *b*-values of 0.58 and 0.59 at the oxidation peak 1 (Fig. 4e), and *b*-values of 0.70 and 0.72 at the reduction peak 2, respectively (Fig. 4f). These values lie between 0.5 and 1, indicating that sodium storage within the hard carbons is governed by a hybrid mechanism involving both ion diffusion and capacitive reactions. A higher *b*-value of W-20%-1100 than that of W-1100 indicates the faster reaction kinetics of the former in both the diffusion-controlled plateau capacity and capacitance-controlled slope capacity. It is known that the slope region is mainly governed by the capacitive control, whilst diffusion control determines the plateau region[38]. As the scanning rate varies, the capacitance ratios of W-1100 are 7.83%, 10.38%, 13.23%, 16.73% and 20.59%, respectively (Fig. 4g and S14), whereas these of W-20%-1100 are 9.39%, 12.51%, 15.89%, 19.68% and 24.11%, respectively (Fig. 4h and S15). Compared to W-1100, W-20%-1100 exhibits enhanced capacitance ratios across all scan rates, suggesting its faster reaction kinetics in the slope region. The storage kinetics of Na^+ were further investigated by EIS (Fig. 4i), which was fitted with an equivalent circuit diagram (Fig. S16). Generally, Nyquist plots of all sample typically exhibit a semicircle associated with charge transfer and a straight line related to diffusion. It is noteworthy that W-20%-1100 exhibits a lower charge transfer resistance (R_{ct}) and a lower Warburg impedance coefficient (σ) (Eq. 3) compared to those of W-

Table 2 Comparison of the sodium storage capacity and cycling stability of W-20%-1100 with the literature data of wood-derived hard carbons

Material	Specific capacity and ICE	Cycle life and capacity retention rate	Ref.
MCC-1400	312 mAh g^{-1} (0.02 A g^{-1}), 82.2%	60 mAh g^{-1} after 1000 cycles (0.5 A g^{-1}), 86.4%	[30]
HC-a	314 mAh g^{-1} (0.05 A g^{-1}), 66.6%	250 mAh g^{-1} after 100 cycles (0.1 A g^{-1}), 78.2%	[31]
BHC-1400	296 mAh g^{-1} (0.05 A g^{-1}), 64.2%	250 mAh g^{-1} after 1000 cycles (1.0 A g^{-1}), 74.6%	[32]
EU1300M	260 mAh g^{-1} (0.02 A g^{-1}), 74.6%	115 mAh g^{-1} after 500 cycles (1.0 A g^{-1}), 72.8%	[33]
HC-1400	313 mAh g^{-1} (0.03 A g^{-1}),85.9%	243 mAh g^{-1} after 500 cycles (0.3 A g^{-1}), 92%	[34]
SCB-1300	206 mAh g^{-1} (0.03 A g^{-1}), 70.5%	206 mAh g^{-1} after 700 cycles (0.15 A g^{-1}), 95.7%	[35]
W-20%-1100	326 mAh g^{-1} (0.03 A g^{-1}), 71.8% 270 mAh g^{-1} (1.0 A g^{-1})	207 mAh g^{-1} after 300 cycles (1.0 A g^{-1}), 76.7%	This study

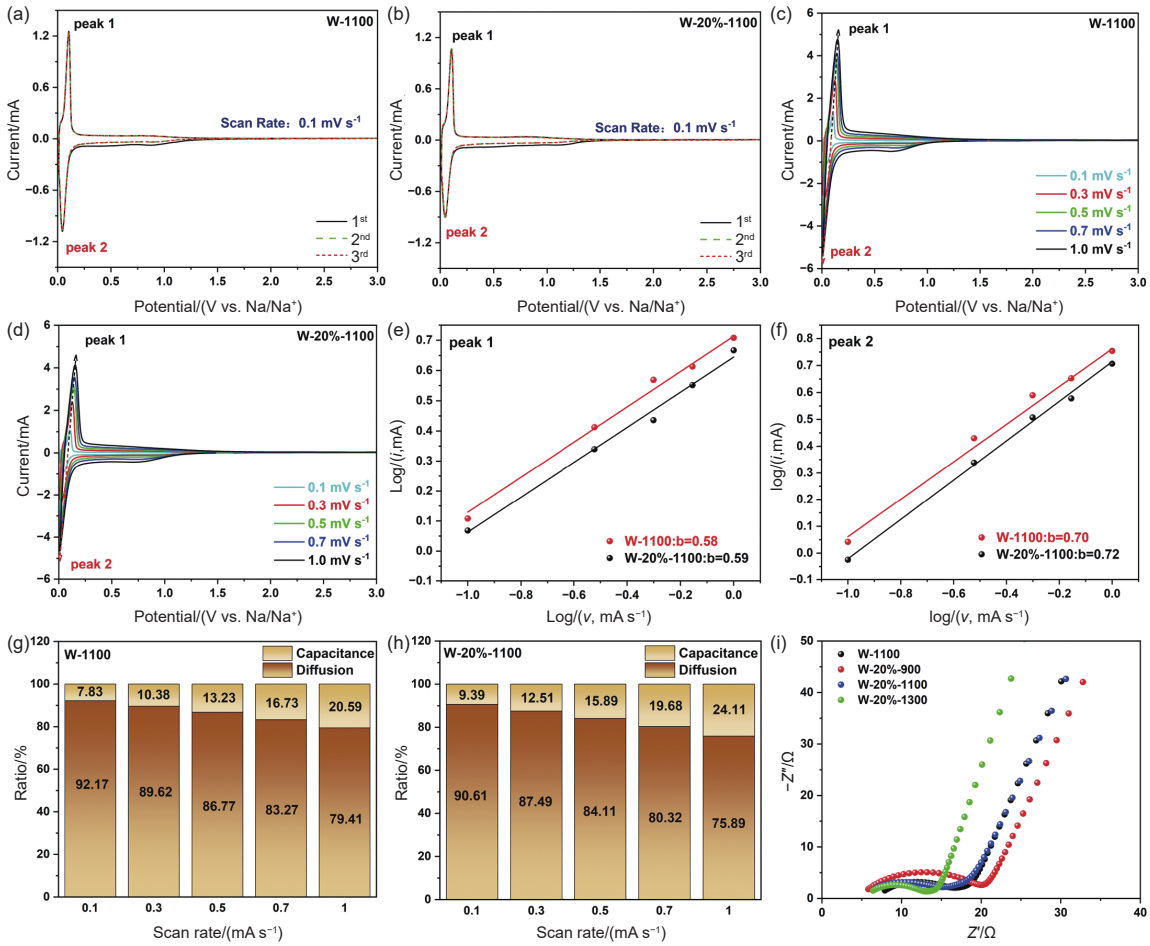

Fig. 4 The initial three CV curves of (a) W-1100 and (b) W-20%-1100 at a scan rate of 0.1 mV s^{-1}. CV curves of (c) W-1100 and (d) W-20%-1100 at different scan rates. Relationship between lg(v) and lg(i) of (e) peak 1 and (f) peak 2. Capacitance ratios of (g) W-1100 and (h) W-20%-1100 at different scan rates. (i) EIS of different samples

1100. The lowest R_{ct} and σ values of W-20%-1300 among all samples can be related to the increased graphitization at its highest carbonization temperature.

$$Z' = R_s + R_{ct} + \sigma\omega^{-\frac{1}{2}} \quad (3)$$

To understand the dynamics of the electrode process, the electrochemical reaction processes of the samples were characterized by GITT (Fig. 5a), where the Na^+ diffusion coefficient (D_{Na^+}) were further calculated using a simplified form of the equation based on Fick's second law (Eq. S3). In general, the slope region shows adsorption of sodium ions due to the surface defects and open pores, while the plateau region with closed pores and pseudo-graphite refers to diffusion[39]. D_{Na^+} remains relatively stable when the voltage is >0.5 V, while in the range of 0.5–0.1 V it first decreases and then increases. This can be attributed to the shift in sodium ion adsorption from the surface to the defect sites[40-41]. The sharp decrease of D_{Na^+} at around 0.1 V indicates the electrochemical reactions transform from surface-controlled process (the slope region) to diffusion-controlled process (the plateau region)[28]. To investigate the sodium storage mechanism of the samples, in-situ Raman spectroscopy was employed to characterize the electrochemical reaction mechanisms and microstructural changes in the samples during charge-discharge cycles (Fig. 5c and 5d). The in-situ Raman spectra of both W-1100 and W-20%-1100 exhibit similar variations, suggesting similar sodium storage behaviors. However, a slight difference can be found if one looks carefully. To be specific, W-1100 shows pronounced D-band throughout the slope region (Fig. S17), while a gradual diminish of the band is observed at 0.5 V for W-20%-1100. It is known that the reduction of the D-band is from the inhibited carbon rings breathing vi-

bration due to Na^+ adsorption on the surface defects and open pores[42-43]. Therefore, the earlier diminish of the *D*-band of W-20%-1100 further confirms its rich defects and open porous structure. The *G* bands of both W-1100 and W-20%-1100 undergo a red shift as sodiation progresses, which can be attributed to the electron transfer induced by the weakening and elongation of the C—C bond from the intercalated Na^+ within the carbon layer[37, 42]. During subsequent charging cycles, both the *D*-band and *G*-band return to their initial positions and intensities, indicating that the sodiation/desodiation process in the obtained samples is reversible. Therefore, the Na^+ storage process in W-20%-1100 can be divided into the following stages (Fig. 5e): 1) Na^+ adsorption at open pores and defects, 2) Na^+ intercalation into graphite-like interlayers and 3) closed-pore filling of Na^+[44-46].

4 Conclusion

Na_2CO_3 was employed as the pore-forming agent and inexpensive, green and renewable natural linden wood was utilized as the carbon precursor to prepare

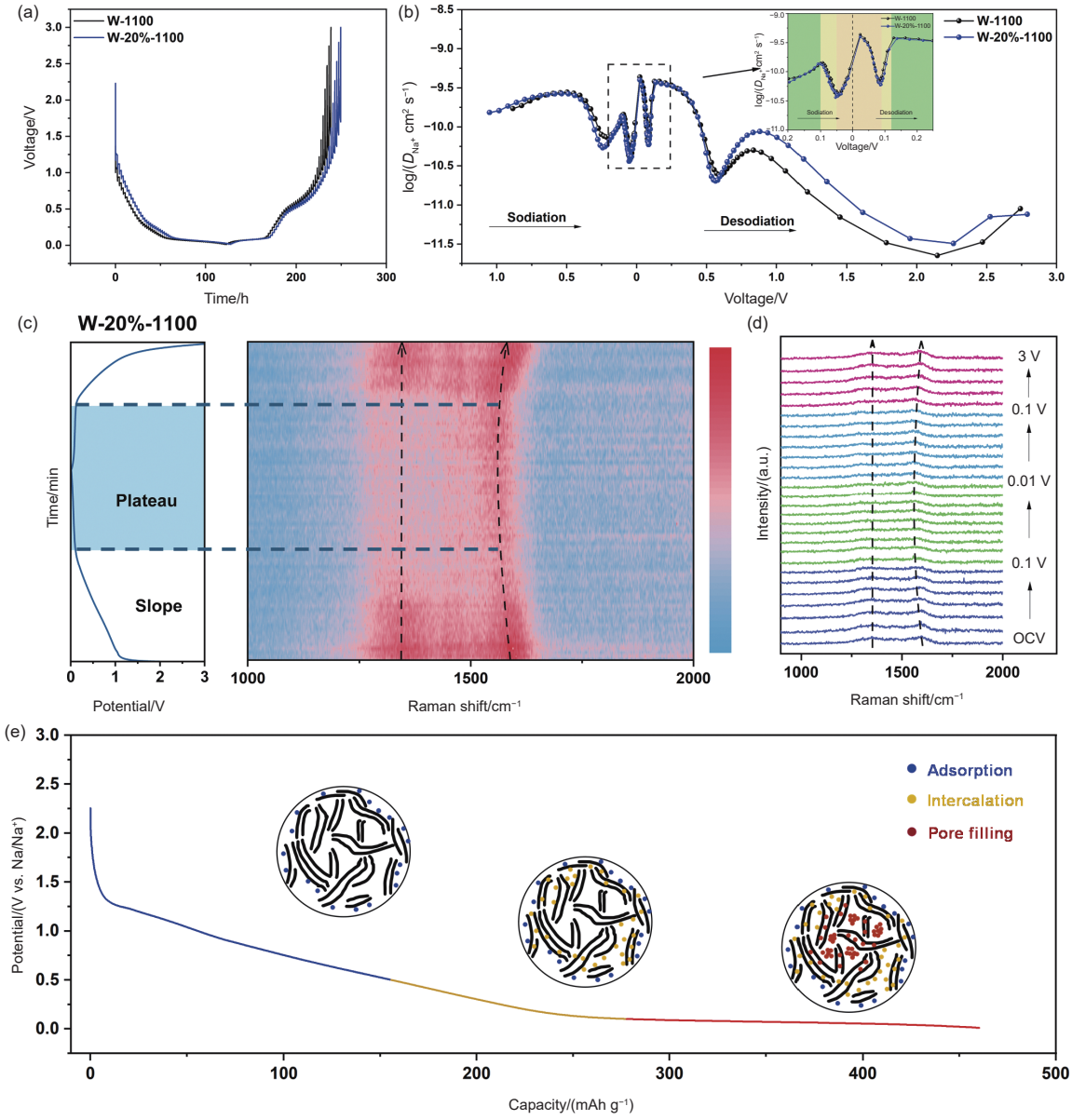

Fig. 5 (a) GITT rate curves for W-1100 and W-20%-1100 during charge-discharge cycles. (b) Changes in D_{Na^+} during sodium insertion and extraction for W-1100 and W-20%-1100. (c) Time-potential evolution of in-situ Raman spectra for W-20%-1100 at 0.3 A/g. (d) In-situ Raman spectra of W-20%-1100 at 0.3 A g^{-1}. (e) Schematic diagram of the Na^+ storage stages of W-20%-1100

hard carbon with an optimized pore structure. Interestingly, it is found that in comparison with W-1100, although the plateau capacity of W-20%-1100 is not changed obviously, W-20%-1100 with abundant open-pores and large interlayer spacing exhibits high slope capacity, which is supposed to be beneficial for efficient sodium ion transport and storage. As an anode material for SIBs, W-20%-1100 exhibits a high specific capacity of 326 mAh g^{-1}. Moreover, it shows outstanding cycling performance and rate capability. After 300 cycles at a current density of 1.0 A g^{-1}, it retains 76.7% of its initial capacity, with a reversible capacity of 270 mAh g^{-1}. At a high current density (10 A g^{-1}), a capacity of 68 mAh g^{-1} is still maintained after 300 cycles. Furthermore, based on the in-situ Raman spectroscopy and GITT results, the sodium storage mechanism in the hard carbon was revealed to follow an "adsorption-intercalation-pore filling" process. Therefore, the present work suggests a strategy to modulate the open pore structure of hard carbons with enhanced slope capacities for high-performance SIBs.

References

[1] Dou X, Hasa I, Saurel D, et al. Hard carbons for sodium-ion batteries: structure, analysis, sustainability, and electrochemistry [J]. Materials Today, 2019, 23: 87-104.

[2] Shen H R, Han X Y, Zheng X M, et al. One-step electrochemical synthesis and optimization of Sb-Co-P alloy anode for sodium ion battery[J]. Electrochimica Acta, 2023, 438: 141529.

[3] Thottungal A, Surendran A, Enale H, et al. Biphasic layered transition metal oxides as positive electrode materials for sodium-ion battery: An emerging strategy for enhancement of electrochemical performance[J]. Journal of Energy Storage, 2025, 131: 115808.

[4] Li Z, Yang Y, Wen B, et al. Recovered cobalt-nickel sulfide from spent lithium-ion batteries as an advanced anode material toward sodium-ion batteries[J]. Journal of Alloys and Compounds, 2023, 956: 170328.

[5] Li X, Ding C, Liang Q, et al. Progress in hard carbons for sodium-ion batteries: Microstructure, sodium storage mechanism and initial Coulombic efficiency[J]. Journal of Energy Storage, 2024, 98: 112986.

[6] Chu Y, Zhang J, Zhang Y, et al. Reconfiguring hard carbons with emerging sodium-ion batteries: A perspective[J]. Advanced Materials, 2023, 35(31): 2212186.

[7] Li W, Nazhipkyzy M, Bandosz T J. Inorganic matter in rice husk derived carbon and its effect on the capacitive performance[J]. Journal of Energy Chemistry, 2021, 57: 639-649.

[8] Liu F, Wang K, Yu S, et al. Enhancing sodium storage performance of biomass-derived hard carbon via hydrothermal carbonization[J]. Journal of Electroanalytical Chemistry, 2025, 976: 118754.

[9] Zhao T, Yan L, Song L, et al. The latest research progress on closed pore hard carbon for sodium-ion batteries[J]. Journal of Energy Storage, 2024, 102: 114209.

[10] Ge Z, Chen X, Hao X, et al. Wood-derived density-adjustable hierarchical porous carbon frameworks for high-performance lithium-sulfur batteries[J]. Materials Letters, 2023, 331: 133537.

[11] Huang J, Li E, Dai B, et al. Regulating the active hydroxyl group of starch: Revealing the evolution of hard carbon structure and sodium storage behavior[J]. Carbon, 2024, 229: 119527.

[12] Song Z, Du Q, Chen J, et al. Joule heating for structure reconstruction of hard carbon with superior sodium ion storage performance[J]. Chemical Engineering Journal, 2024, 496: 154103.

[13] Tao H, Zhou M, Wang K, et al. Glycol derived carbon- TiO_2 as low cost and high performance anode material for sodium-ion batteries[J]. Scientific Reports, 2017, 7(1): 43895.

[14] Ji Y, Li S, Yuan T, et al. Enhancing the sodium storage performance of hard carbon by constructing thin carbon coatings via esterification reactions[J]. Journal of Colloid and Interface Science, 2025, 677: 719-728.

[15] Zhang Y, Zhang N, Chen W, et al. Effect of vapor carbon coating on the surface structure and sodium storage performance of hard carbon spheres[J]. Energy Technology, 2019, 7(11): 1900779.

[16] Wang Y, Li M, Zhang Y, et al. Hard carbon for sodium storage: Mechanism and performance optimization[J]. Nano Research, 2024, 17(7): 6038-6057.

[17] Yang Z, Xue H, Zhang Y, et al. Ni_3S_2-modified nan-wood hard carbon for enhanced SIBs[J]. Journal of Energy Storage, 2025, 129: 117377.

[18] Zheng Y, Lu Y, Qi X, et al. Superior electrochemical performance of sodium-ion full-cell using poplar wood derived hard carbon anode[J]. Energy Storage Materials, 2019, 18: 269-279.

[19] Huang C, Yin J, Shi W, et al. Recent advances of tailoring defects and pores in hard carbon for sodium storage[J]. Materials Today Energy, 2024, 40: 101501.

[20] You S, Zhang Q, Liu J, et al. Hard carbon with an opened pore structure for enhanced sodium storage performance[J]. Energy & Environmental Science, 2024, 17(21): 8189-8197.

[21] Feng B, Xu L, Yu Z, et al. Wood-derived carbon anode for sodium-ion batteries[J]. Electrochemistry Communications, 2023, 148: 107439.

[22] Luo J, Yao X, Yang L, et al. Free-standing porous carbon electrodes derived from wood for high-performance Li-O_2 battery applications[J]. Nano Research, 2017, 10(12): 4318-4326.

[23] Zheng Z, Hu S, Yin W, et al. CO_2-etching creates abundant closed pores in hard carbon for high-plateau-capacity sodium storage[J]. Advanced Energy Materials, 2024, 14(3): 2303064.

[24] Olmos F, Hennessy B P, Manousiouthakis I V, et al. Thermodynamic feasibility analysis of a water-splitting thermo-chemical cycle based on sodium carbonate decomposition[J]. International Journal of Hydrogen Energy, 2019, 44(8): 4041-4061.

[25] Qiu C, Li A, Qiu D, et al. One-step construction of closed pores enabling high plateau capacity hard carbon anodes for sodium-ion batteries: closed-pore formation and energy storage mechanisms[J]. ACS Nano, 2024, 18(18): 11941-11954.

[26] Hu X, Qu Z, Dai Y, et al. Concurrent multifactorial engineering of closed-pore hard carbon architectures with optimized crystallographic spacing for advanced sodium storage[J]. Journal of Power Sources, 2025, 655: 237978.

[27] Qiu G, Miao Z, Guo Y, et al. Bamboo-based hierarchical porous carbon for high-performance supercapacitors: the role of different components[J]. Colloids and Surfaces A: Physicochemical and Engineering Aspects, 2022, 650: 129575.

[28] Hou Z, Zhao Y, Du Y, et al. Expediting sodium energy of hard carbon by cation/anion Co-interfering chemistry[J]. Advanced Functional Materials, 2025, 35(36): 2505468.

[29] Feng X, Li Y, Li Y, et al. Unlocking the local structure of hard carbon to grasp sodium-ion diffusion behavior for advanced sodium-ion batteries[J]. Energy & Environmental Science, 2024, 17(4): 1387-1396.

[30] Wu X S, Dong X L, Wang B Y, et al. Revealing the sodium storage behavior of biomass-derived hard carbon by using pure lignin and cellulose as model precursors[J]. Renewable Energy, 2022, 189: 630-638.

[31] Chen B, Zhong L, Lu M, et al. Lignin molecular sieving engineering enables high-plateau-capacity hard carbon anodes for sodium-ion batteries[J]. Green Chemistry, 2024, 26(13): 7919-7930.

[32] Huang J, Liu D, Huang Z, et al. Sustainable Balsa wood-derived high-rate hard carbon anodes for sodium-ion hybrid capacitors[J]. Journal of Power Sources, 2024, 613: 234863.

[33] Sun S, Wang L. Eucommia ulmoides barks-derived anodes for sodium ion battery and method to improve electrochemical performances by modifying Defects[J]. Electronic Materials Letters, 2024, 20(4): 474-483.

[34] Xu J, Chen B, Hu B, et al. 3D connected porous structure hard carbon derived from paulownia xylem for high rate performance sodium ion battery anode[J]. Journal of Energy Storage, 2024, 81: 110306.

[35] Liao J, Qiu H, Zhou P, et al. Unraveling the effect of the microstructure of agricultural waste plants-derived hard carbons on the sodium storage performance[J]. Fuel, 2024, 376: 132664.

[36] Liu J, You Y, Huang L, et al. Precisely tunable instantaneous carbon rearrangement enables low-working-potential hard carbon toward sodium-ion batteries with enhanced energy density[J]. Advanced Materials, 2024, 36(44): 2407369.

[37] Li C, Wang H, Lei C, et al. Preparation and study on the storage sodium performance of coumarone resin/petroleum asphalt composite hard carbon anode material[J]. Journal of Energy Storage, 2025, 120: 116477.

[38] Wen T, Xu Z, Yang P, et al. Low-cost scalable lignite-epoxy resin cross-linked hard carbon for sodium-ion battery anodes[J]. Electrochimica Acta, 2025, 537: 146881.

[39] Lai H, Zhang S, Wang Q, et al. Microporous structure engineering of hard carbon through synergistic catalytic dehydration and activation for enhanced sodium ion storage[J]. Nano Energy, 2025, 143: 111298.

[40] Yan Y, Liu W, Qu M, et al. Molten salt-engineered sucrose-derived hard carbon with tailored nanoarchitecture for superior sodium-ion storage[J]. Journal of Energy Storage, 2025, 132: 117697.

[41] Sun Z, Li Z, Li Y, et al. Unveiling a two-stage closed-pore formation mechanism in bamboo-derived hard carbons for high-plateau-capacity sodium-ion battery anodes[J]. Chemical Engineering Journal, 2025, 521: 167011.

[42] Zhang Q, Yuan F, Sun Q, et al. Reasonable regulation of carbon layers and micropores to promote the extreme capacity of hard carbons for sodium-ion batteries[J]. Applied Surface Science, 2024, 664: 160277.

[43] Yang J, Ren Q, Sun Z, et al. Regulating closed-pore concentration of hard carbon for ultrahigh plateau capacity sodium-ion batteries[J]. Energy Storage Materials, 2025, 82: 104574.

[44] Shen Y, Wang Y, Li H, et al. Air-stabilization creates non-crosslinked starch particles for high-performance hard carbon anodes[J]. Advanced Functional Materials, 2025: e09126.

[45] Zhao X, Shi P, Wang H, et al. Unlocking plateau capacity with versatile precursor crosslinking for carbon anodes in Na-ion batteries[J]. Energy Storage Materials, 2024, 70: 103543.

[46] Xu C, Zhang D, Ma G, et al. Pre-carbonization facilitates closed pore formation in asphalt-derived hard carbon for high-plateau-capacity sodium storage[J]. Chemical Engineering Journal, 2025, 520: 166398.